Porous C_3N_4 Nanolayers@N-Graphene Films as Catalyst Electrodes for Highly Efficient Hydrogen Evolution

Jingjing Duan,[†] Sheng Chen,[†] Mietek Jaroniec,[‡] and Shi Zhang Qiao*,[†]

[†]School of Chemical Engineering, The University of Adelaide, Adelaide, South Australia 5005, Australia and [‡]Department of Chemistry and Biochemistry, Kent State University, Kent, Ohio 44240, United States

ABSTRACT Pt-free electrocatalysts for hydrogen evolution reaction (HER) with high activity and low price are desirable for many state-of-the-art renewable energy devices, such as water electrolysis and photoelectrochemical water splitting cells. However, the design and fabrication of such materials remain a significant challenge. This work reports the preparation of a flexible three-dimensional (3D) film by integrating porous C_3N_4 nanolayers with nitrogen-doped graphene sheets, which can be directly utilized as HER catalyst electrodes without substrates. This nonmetal electrocatalyst has displayed an unbeatable HER performance with a very positive onset-potential close to that of commercial Pt (8 mV *vs* 0 mV of Pt/C, *vs* RHE @ 0.5 mA cm^{-2}), high exchange current density of 0.43 mA cm^{-2}, and remarkable durability (seldom activity loss >5000 cycles). The extraordinary HER performance stems from strong synergistic effect originating from (i) highly exposed active sites generated by introduction of in-plane pores into C_3N_4 and exfoliation of C_3N_4 into nanosheets, (ii) hierarchical porous structure of the hybrid film, and (iii) 3D conductive graphene network.

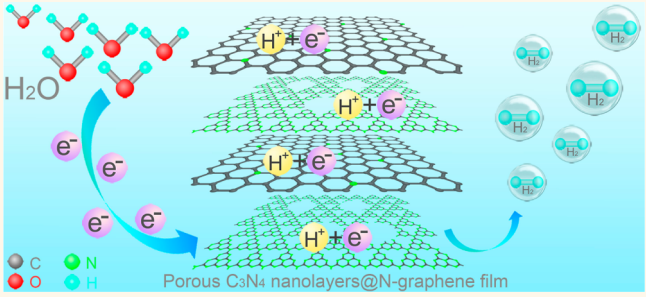

KEYWORDS: two-dimensional materials · hydrogen evolution reaction · carbon nitride nanolayers · nitrogen doped graphene · van der Waals heterostructure

As one of the most abundant elements on the earth, hydrogen is considered to be the future substitute for finite fossil fuels.[1] Although hydrogen may be generated from water, biomass, or coal, only hydrogen derived from water splitting can provide a sustainable, secure and clean energy system without environmental emission.[2−5] Water electrolysis *via* hydrogen evolution reaction (HER), promoted by effective electrocatalysts, can generate hydrogen at room temperature. In particular, the most efficient HER electrocatalyst, *i.e.*, platinum (Pt), can produce hydrogen from water without the need of excessive driving potentials (onset-potential is about 0 mV *vs* RHE).[6−8] Nevertheless, Pt is neither abundant nor low cost, which are the main drawbacks in the development of water electrolysis technology for large-scale hydrogen production. Therefore, it is both practically necessary and economically desirable to develop an alternative HER catalyst with similar activity but much lower price as compared to commercial Pt/C.[9−11]

For that reason, extensive efforts have been undertaken to develop non-Pt electrocatalysts, including both nonprecious metal (MoS_2, CoP, Ni−Mo, *etc.*) and nonmetal materials (boron-doped graphene, *etc.*).[12−14] However, the catalytic activities of these materials are inferior to Pt/C with very large overpotentials (usually >100 mV for nonprecious metal, and >200 mV for nonmetal materials @ 10 mA cm^{-2}). The common strategies used for enhancing the performances of HER electrocatalysts include the optimization of their chemical compositions and/or microstructures. Another approach is to hybridize catalytically active species with other components such as various carbons (porous carbons, CNTs, graphene, *etc.*). Recently, there is a great interest in the study of nanohybrids named "van der Waals heterostructures", which are typically composed of graphene and other two-dimensional (2D) nanolayers assembled

* Address correspondence to s.qiao@adelaide.edu.au.

Received for review November 24, 2014 and accepted January 5, 2015.

Published online January 05, 2015
10.1021/nn506701x

alternatively in a layer-by-layer fashion.[15] Generally, this kind of hybrid can exhibit an improved electrocatalytic activity due to the excellent structural features such as highly exposed active centers present on 2D nanolayers, conductive graphene sheets, as well as strong synergistic effects between these components. Indeed, we recently prepared a nanocomposite consisting of g-C_3N_4 and graphene with the structure similar to van der Waals heterostructures, which exhibited a good HER activity as evidenced by the overpotential shifted from >700 mV for individual g-C_3N_4 to ~250 mV for graphene-C_3N_4 (*vs* RHE @ 10 mA cm^{-2}).[16] Despite great efforts in this research, the study of electrocatalysts based on van der Waals heterostructures is still in its infant stage. From the viewpoint of practical applications further work is needed to enhance their electrocatalytic activities, making them comparable to that of commercial Pt/C.

Very recently, we demonstrated that various parameters other than chemical components and microstructure can contribute to the formation of an active electrocatalyst, for example, electrode architecture, mechanical properties and catalyst/substrate contact. Currently, electrocatalysts are often prepared in the form of powders (including our previous work devoted to graphene-C_3N_4 composite). They are dispersed in solvents, casted onto electrodes or substrates, and then dried to assemble into membrane electrode.[17,18] This process usually results in a limited catalyst/electrolyte contact area and unavoidable powder agglomeration, which greatly compromise the electrocatalytic performance. In contrast, three-dimensional (3D) macroscopic assemblies, which can be directly utilized as catalyst electrodes with sufficient catalyst/electrode contact area and good mechanical properties, could be a promising solution to this problem.[19,20] Among various materials, nitrogen (N)-doped graphene films are ones of the most promising components for fabrication of 3D self-supported electrocatalysts because of their good conductivity, flexibility and catalytic properties.[21−24] In particular, numerous out-of-plane pores between graphene sheets in a 3D film can provide continuous porosity for mass transport during electrochemical processes, which is highly advantageous for achieving the desired electrocatalytic HER performance.[25,26] On the other hand, it is well-known that the amount of accessible active centers is directly related to the catalytic performance. As in the case of other well-studied electrocatalysts such as MoS_2, the defects and edges of g-C_3N_4 are important catalytic centers for HER, which are active for water dissociation ($2H_2O \rightarrow 2H_2 + O_2$). In this respect, the generation of in-plane pores can introduce additional edges and defects in 2D C_3N_4 nanolayers, and consequently provide more active sites for HER. Therefore, a rational assembly of N-doped graphene with porous C_3N_4 (denoted as PCN) nanolayers into a 3D free-standing film may form a new class of cheap yet efficient electrocatalysts that are useful in many energy-related catalytic reactions. To our best knowledge, the reports devoted to N-doped graphene and PCN hybrid films for HER are rare.

In this paper, we fabricate such a 3D hybrid film by integrating intentionally 2D porous g-C_3N_4 nanolayers with N-doped graphene sheets (denoted as PCN@N-graphene film) *via* a simple vacuum filtration method. This material has an interesting structure comparable to previously reported van der Waals heterostructures, but with a 3D macroscopic architecture. As compared to its 2D counterpart, this 3D heterostructure has many intriguing properties for favored catalysis, such as highly exposed catalytic centers, hierarchical pores, and strong mechanical flexibility. Electrochemical study shows that this nonmetal material exhibits a superior HER catalytic activity with a low overpotential very close to that of commercial Pt/C (80 mV *vs* 4 mV), which outperforms all the previously reported nonmetal electrocatalysts (>200 mV *vs* RHE) and most nonprecious metal catalysts. To investigate the origin of such high performance, the morphology, microstructure and composition of the film have been characterized by a number of techniques.

RESULTS AND DISCUSSION

Morphology, Composition and Structure of Catalysts. The multistep preparation process of PCN nanolayers@N-graphene film is displayed in Scheme 1. First, the mixture of melted cyanamide and SiO_2 template was annealed in N_2, and then PCN was obtained by etching SiO_2 template with NaOH. The scanning electron microscopy (SEM) image of SiO_2 template is shown in Figure 1a, as can be seen in this image SiO_2 spheres of about 120 nm are regularly packed. As expected the SEM and transmission electron microscopy (TEM) images show regularly arranged pores of about 120 nm in PCN (Figures 1b, S1a, Supporting Information). The X-ray diffraction (XRD) pattern of PCN can be assigned to g-C_3N_4 (Figure S1b); its Fourier transform infrared (FTIR) spectrum displays typical stretching modes of CN heterocycles (1200−1650 cm^{-1}) and the breathing mode of triazine units (805 cm^{-1}, Figure S1c).

Second, water is utilized to exfoliate PCN because the similar surface energy of water (102 mJ m^{-2}) and g-C_3N_4 (115 mJ m^{-2}) and the easy formation of hydrogen bonds between them facilitate the exfoliation.[27] As a result, thin, transparent and corrugated PCN nanolayers with macropores were successfully prepared by bath-sonicating PCN in water without any additives or preintercalation steps (Figures 1c, S1d). The thickness of PCN nanolayers measured by atomic force microscopy (AFM) is 1.3−1.4 nm, displaying less than 4 layers of g-C_3N_4 since its interlayer spacing is 0.33 nm (Figure 1d). For the purpose of comparison

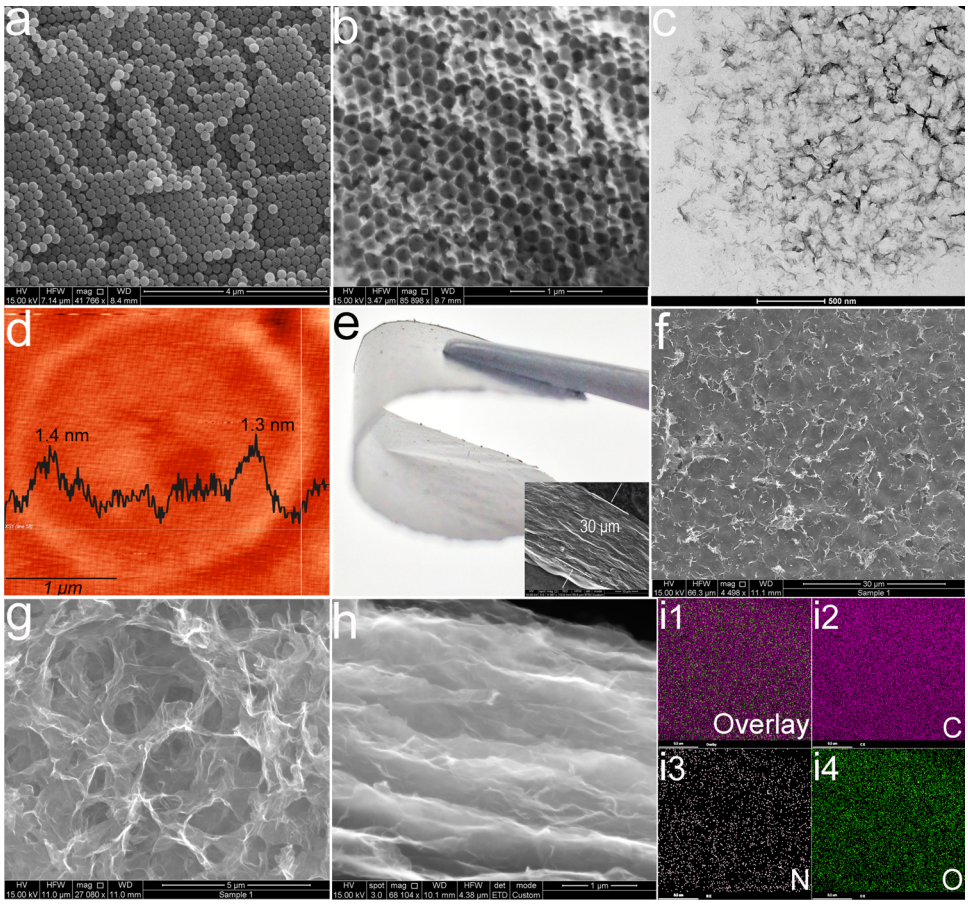

Figure 1. (a) SEM image of packed SiO_2 spheres, (b) SEM image of PCN, (c, d) TEM and AFM images of PCN nanolayers, inset in (d) is the height distribution curve; (e) Photograph of PCN@N-graphene film, inset shows the SEM image of the cross-section view, (f, g, h) SEM images of the surface, inside structure, cross-section view at high magnification, (i1−i4) EDS elemental mapping images of overlay, C, N and O of (h).

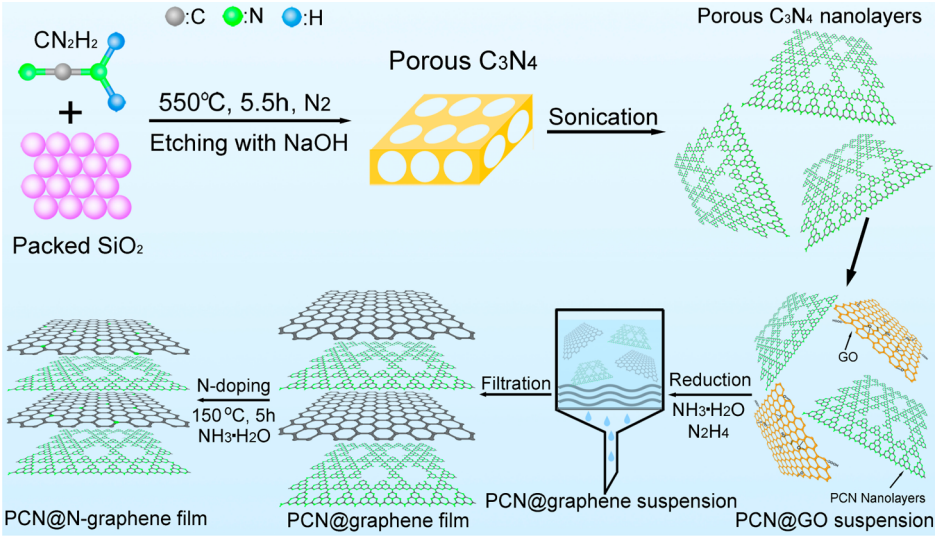

Scheme 1. Schematic illustration of the preparation process of PCN@N-graphene film.

bulk C_3N_4 without pores and the corresponding nanolayers (about 1.9 nm, less than 5 layers) were also synthesized and characterized (Figure S2).

Third, PCN nanolayers were mixed with graphene oxide (GO) and the resulting mixture (denoted as PCN@GO suspension) was reduced by hydrazine (denoted as PCN@graphene suspension) before filtration to obtain the PCN@graphene film. The nanosheets in the mixed suspension are prone to deposit on the filter membrane in a near-parallel manner directed by

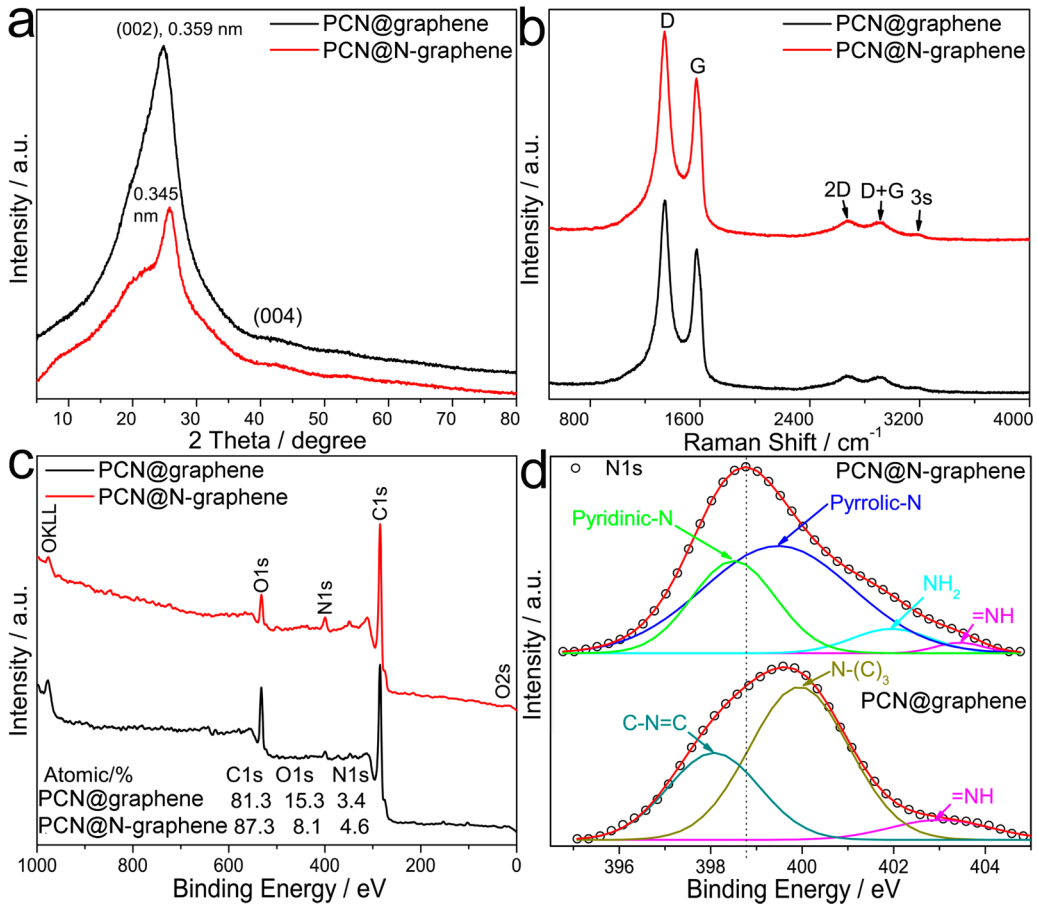

Figure 2. (a) XRD patterns, (b) Raman spectra, (c) XPS survey scans and (d) high resolution N 1s XPS spectra of PCN@graphene film and PCN@N-graphene film.

vacuum suction. They are held together by interlayer $\pi-\pi$ interactions, van der Waals forces and hydrogen bonding of oxygen-containing groups but kept separated by the hydration forces, electrostatic repulsion and corrugated configuration of 2D nanosheets.[10c,10d] Lastly, PCN@graphene film was subjected to a solvothermal process in ammonia to obtain the nitrogen doped film (PCN@N-graphene film). The freeze-dried PCN@N-graphene is a highly flexible self-supported film with a metallic luster, having diameter of 37 mm and thickness of 30 μm (Figures 1e and S3a). The top surface is microcorrugated with pores (Figure 1f). Inside the film, there are hierarchical pores ranging from tens of nanometers to several micrometers intra and inter layers, resulting from the cross-linking of graphene sheets and PCN nanolayers (Figure 1g). From the cross-section view at high magnification, a layer-by-layer alternate structure is visible (Figure 1h). The energy dispersive X-ray spectroscopy (EDS) elemental mapping from this area displays homogeneous distribution of C, N and O (Figure 1i1−i4); and the EDS spectrum shows an N percentage of 5.36 at %, which originates from C_3N_4 and N-graphene (Figure S3b). The nondoped PCN@graphene film has similar microstructure, but with a thickness of 75 μm (Figure S4a−c). The decreased thickness after nitrogen doping is because of the agglomeration of graphene sheets at elevated temperature and high pressure of the N-doping process. Its EDS spectrum gives N percentage of 3.83 at % only from C_3N_4, lower than that of N-doped film (Figure S4d); and the distribution of C and N confirms this feature, in which N distribution is much less dense than that of PCN@N-graphene film (Figure S4e,f).

The microstructure and interactions between N-graphene sheets and PCN nanolayers in the film were characterized by XRD and Raman spectra. The XRD pattern of PCN@N-graphene film shows a negligible (004) peak at 42.5°, and an intense (002) peak at 24.8° with an interlayer spacing ($d_{(002)}$) of 0.345 nm, which are originated from graphene (Figure 2a). Due to agglomeration of graphene sheets during N-doping, the $d_{(002)}$ spacing is smaller than that of PCN@graphene film (0.359 nm at 25.8°), but larger than that of pristine graphite (0.335 nm) because of the corrugated 2D microstructure and interlayer repulsive forces.[23,24] The peak shift (from 25.8° to 24.8°) may be related to the structure and valence change of carbon in the hybrid films after N-doping. The XRD patterns of graphene film and N-graphene film (Figure S5) also display a peak shift and $d_{(002)}$ reduction (from 0.395 nm

at 22.2° of graphene film to 0.363 nm at 24.4° of N-graphene film) after N-doping, confirming N-doping effect in as-prepared films. Unexpectedly, the XRD peak position changes and the $d_{(002)}$ spacing decreases after incorporating PCN nanolayers in the film, probably because there is a strong coupling between PCN nanolayers and N-graphene/graphene sheets through residual oxygen-containing functional groups. This coupling in the heterostructure compromises the interlayer repulsive forces, thus affecting the carbon hybridization state and interlayer distance of graphene sheets.

The Raman spectra (Figure 2b) of PCN@graphene and PCN@N-graphene films display the D band (1344 cm^{-1}), G band (1574 cm^{-1}), 2D band (2672 cm^{-1}), D+G band (2920 cm^{-1}), and 3s band (3195 cm^{-1}) from carbon.[28] Similar peaks are visible on the Raman spectra of graphene and N-graphene films (Figure S6). The I_D/I_G peak intensity ratios obtained for graphene, N-graphene, PCN@graphene and PCN@N-graphene films are 1.18, 1.30, 1.12 and 1.26, respectively, suggesting the presence of numerous defects and disorders within the samples. The I_D/I_G ratios increase after N-doping, indicating that the introduction of N onto graphene sheets may increase the sp^3 hybridization of carbon, and the amount of defects and fragments further. Interestingly, the I_D/I_G ratios of as-prepared films decrease slightly after incorporation of PCN nanolayers, indicating possible coupling between PCN nanolayers and N-graphene/graphene *via* defective sites in the heterostructures, which is consistent with XRD results.

The composition and element valence of the heterostructured films before and after N-doping were investigated by X-ray photoelectron spectroscopy (XPS). The XPS survey scans of PCN@gaphene and PCN@N-graphene films indicate the existence of carbon, oxygen and nitrogen (Figure 2c). After N-doping, the N percentage in PCN@N-graphene film is calculated to be 4.6 at %, higher than that of PCN@graphene film (3.4 at %). Moreover, there is a peak shift in N 1s from 399.7 eV (PCN@graphene film) to 398.7 eV (PCN@N-graphene film), revealing a valence and bond change. The deconvolution of N 1s peak visible on the spectrum of PCN@N-graphene film shows nitrogen in the form of pyridinic-N (398.5 eV), pyrrolic-N (399.5 eV), $-NH_2$ (401.9 eV) and =NH (403.4 eV) from N-graphene, C_3N_4 and adsorbed ammonia; while that of N 1s in the case of PCN@graphene film indicates the presence of nitrogen in C=N—C (398.1 eV), N−$(C)_3$ (399.9 eV) and =NH (403.0 eV) from C_3N_4 and adsorbed ammonia (Figure 2d).[29,30] The deconvolution of C 1s spectra of PCN@N-graphene and PCN@graphene films is also displayed in Figure S7; and the reduction of O percentage from 15.3 at % (PCN@graphene film) to 8.1 at % (PCN@N-graphene film) suggests that the oxygen functional groups on graphene sheets were further reduced during N-doping process.

The peaks at 805 cm^{-1} on the FTIR spectra of PCN@graphene and PCN@N-graphene films originate from triazine units of C_3N_4, further confirming the presence of PCN nanolayers in the hybrid films (Figure S8).[28,31] In addition, the PCN@N-graphene film displays a good thermal stability as evidenced by thermogravimetric analysis (TGA), retaining 90.2% of the original mass after heating at 800 °C in N_2 atmosphere, which surpasses that of PCN@graphene film (82.4%, Figure S9).[23]

N_2 adsorption−desorption isotherms were measured to estimate the specific surface area and pore volume of the materials.[32−35] The Brunauer−Emmett−Teller (BET) specific surface area and pore volume obtained for PCN@N-graphene film are 58 $m^2\ g^{-1}$ and 0.14 $cm^3\ g^{-1}$, respectively; these values are lower than the corresponding values, 114 $m^2\ g^{-1}$ and 0.37 $cm^3\ g^{-1}$, estimated for PCN@graphene film (Figure 3a). Both pore size distribution curves (PSD, inset in Figure 3a) are broad ranging from tens of nanometers to over one hundred nanometers, which indicates that the nanosheets (PCN nanolayers and graphene sheets) do not restack in the hybrid films, and form hierarchical porous structure as evidenced by SEM. However, the experimental procedure of N_2 adsorption−desorption measurement involves drying and vacuum degassing at elevated temperatures to clean the samples to obtain reliable data, which can cause substantial aggregation in graphene-based materials.[36] Interestingly, adsorption of methylene blue (MB) from ethanol solutions was shown to be more reliable than N_2 adsorption for evaluating the specific surface area of graphene-based materials because the former method does not need drying, thermal annealing and vacuum degassing processes.[21,36,37] As shown in Figure 3b, the specific surface areas of PCN@graphene and PCN@N-graphene film calculated from MB ultraviolet (UV−vis) absorption curves are 285 $m^2\ g^{-1}$ and 195 $m^2\ g^{-1}$, respectively. The specific surface area of PCN@N-graphene film obtained by MB adsorption is two times higher than that obtained by N_2 adsorption. This method was also used to measure the specific surface areas of N-graphene film (248 $m^2\ g^{-1}$) and graphene film (343 $m^2\ g^{-1}$, Figure S10). Obviously, the decreased specific surface areas of films after N-doping are due to the agglomeration of graphene sheets during N-doping, which is consistent with the decreased thickness and interlayer distance estimated by SEM and XRD analysis. Additionally, the smaller specific surface areas of hybrid films after incorporating PCN nanolayers may be because the strong coupling between PCN nanolayers and N-graphene/graphene sheets reduces repulsive forces, and consequently, the interlayer distance, which agrees well with the XRD and Raman data.

HER Activity and Kinetics. The HER performance was tested in a three-electrode cell (Figure S11) and the

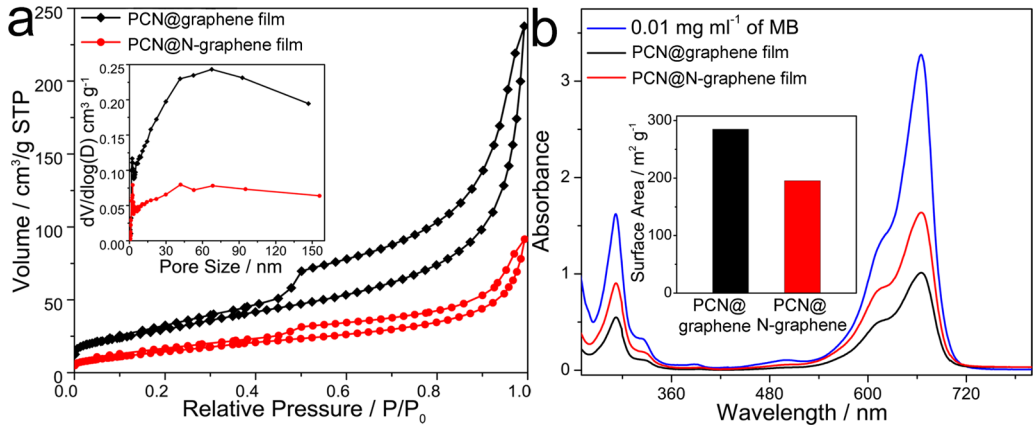

Figure 3. (a) N_2 adsorption−desorption isotherms obtained for PCN@graphene and PCN@N-graphene films, inset shows the corresponding PSD curves; (b) UV−vis absorption spectra of MB solutions before and after adsorption experiments using PCN@graphene and PCN@N-graphene films.

obtained electrochemical parameters are shown in Table S1 (all potentials were referenced to a reversible hydrogen electrode-RHE). The HER polarization curves (*iR* corrected) are displayed in Figure 4a. Significantly, PCN@N-graphene film after initial 750 cyclic voltammetry (CV, denoted as PCN@N-graphene-750) exhibits a very small onset-potential (η_o, defined as the potential to achieve 0.5 mA cm^{-2} of the current density *J*) of −0.008 V *vs* RHE, which is very close to that of commercial Pt on carbon fiber (denoted as Pt/CF, 25% of Pt, E-TEK, Figure S12), and a current density *J* of 50.2 mA cm^{-2} at −0.2 V *vs* RHE ($j_{-0.2}$). This HER activity is much better than that of PCN@N-graphene film without CV cycles, with η_o of −0.011 V and $j_{-0.2}$ of 12.9 mA cm^{-2}, suggesting that the potential cycles can improve the HER activity significantly, which can be further related to the change of interactions between active species and the catalyst electrode during HER processes. While PCN@graphene film features η_o = −0.044 V and $j_{-0.2}$ = 5.0 mA cm^{-2}, which are much lower than those of N-doped hybrid film. The HER activities of heterostructured films are higher than that of both pure graphene and N-graphene films (with *iR* correction, Figure S13). The aforementioned results suggest that the integration of PCN nanolayers with graphene sheets and N-doping can enhance the HER activity significantly; PCN@N-graphene-750 was shown to have the greatest HER activity among as-prepared materials.

Generally, there are three reaction steps for HER in acidic electrolytes, including a primary discharge step (Volmer reaction, with a Tafel slope of 120 mV dec^{-1}) followed by an electrochemical desorption step (Heyrovsky reaction, with a Tafel slope of 40 mV dec^{-1}) or a recombination step of adsorbed hydrogen on catalysts (Tafel reaction, with a Tafel slope of 30 mV dec^{-1}).[2,38,39] The Tafel slope is an inherent property of catalysts determined by the rate- determining step (RDS); a small Tafel slope leads to a greatly enhanced HER rate at a moderate increase of overpotential.[4,40,41]

To investigate the kinetics of HER processes promoted by as-prepared catalysts, the Tafel plots at low overpotentials have been linearly fitted to the Tafel eq (Figure 4b, *iR* corrected). The Tafel plot of PCN@N-graphene-750 gives a Tafel slope of 49.1 mV dec^{-1}, much lower than those of PCN@N-graphene (88.6 mV dec^{-1}) and PCN@graphene films (143.3 mV dec^{-1}). The variation of Tafel slops can be explained by the change of RDS in HER processes. The RDS for PCN@N-graphene and PCN@graphene films follow the Volmer step, but it is the Heyrovsky step is observed for PCN@N-graphene-750. Even though the HER mechanism promoted by the heterostructured films is inconclusive, the smallest Tafel slop of PCN@N-graphene-750 still suggests the most favorable kinetics of HER processes among all the samples, which is also very low as compared to the reported values.[9,11,42]

In addition, the HER activity was further compared quantitatively using the required overpotentials to achieve a current density *J* of 10 mA cm^{-2} (η_{10}, left of Figure 4c). For PCN@N-graphene-750, η_{10} is 0.08 V *vs* RHE, much smaller than those of PCN@N-graphene (0.17 V), PCN@graphene films (0.28 V), confirming high HER activity of PCN@N-graphene-750. The exchange current density (j_0) is also one of the most important parameters to describe the catalytic efficiency.[4,43] By extrapolation of the Tafel plots to *J* axis, the obtained j_0 of PCN@N-graphene-750 is 0.43 mA cm^{-2}, higher than those of PCN@N-graphene (0.37 mA cm^{-2}), and PCN@graphene films (0.25 mA cm^{-2}; right panel of Figure 4c). The highest j_0 of PCN@N-gaphene-750 suggests the best catalytic efficiency, further confirming the most favorable HER kinetics at the PCN@N-graphene-750/electrolyte interface among all the samples, which is also one of the largest values among reported results.[9,11,40,44]

The HER kinetics at the electrode/electrolyte interface was further investigated by electrochemical impedance spectroscopy (EIS, tested at −0.2 V *vs* RHE, Figures 4d, S13d).[6,45] The series resistance (R_s) data was

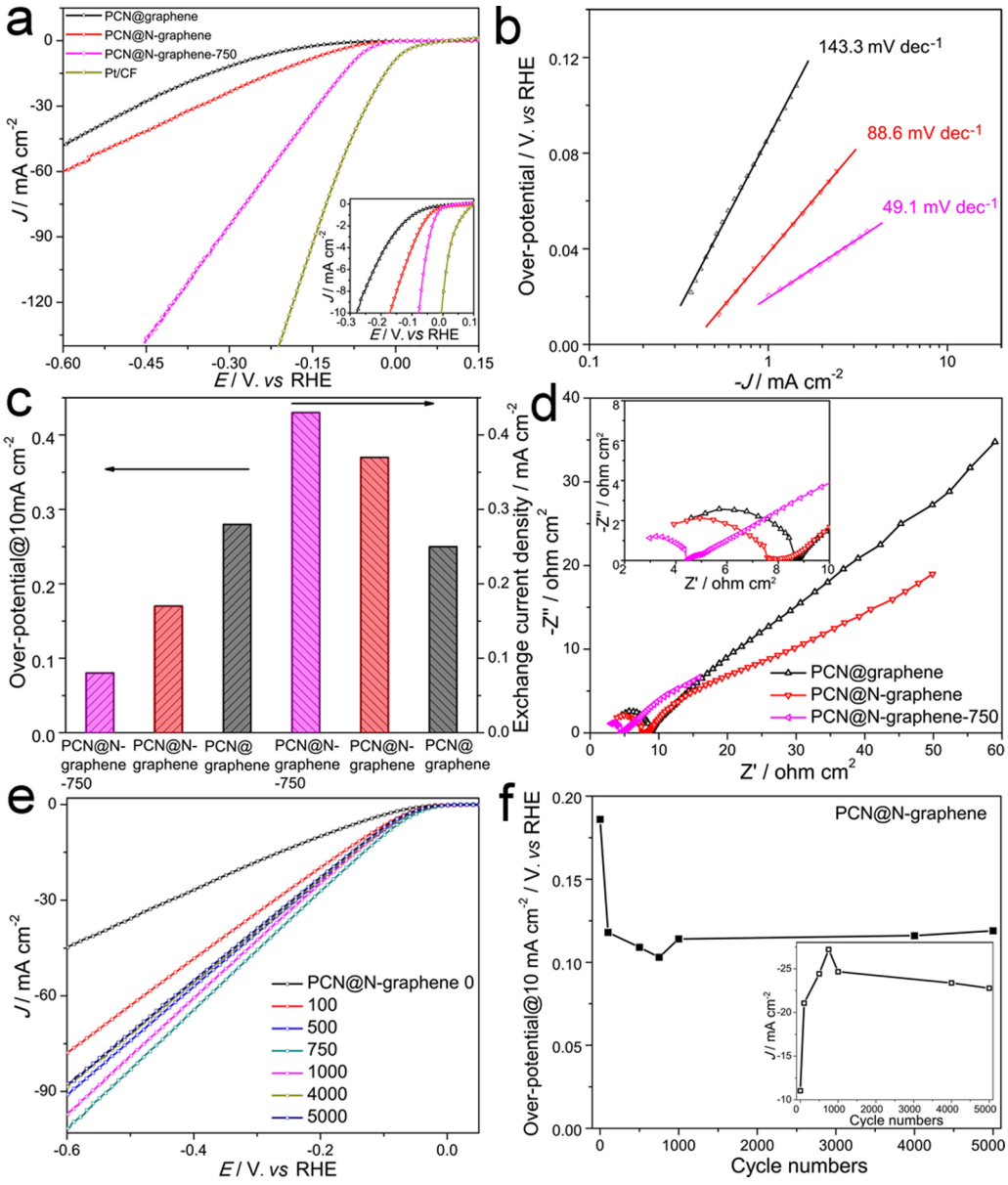

Figure 4. (a) Polarization curves (inset shows polarization curves with current density below 10 mA cm^{-2}). (b) Tafel plots at low potentials. (c) Overpotential@10 mA cm^{-2} *vs* RHE (left) and exchange current density (right). (d) Electrochemical impedance spectra at −0.2 V *vs* RHE of PCN@graphene, PCN@N-graphene, and PCN@N-graphene-750 films. (e) The polarization curves after different CV cycles. (f) Required overpotential@10 mA cm^{-2} *vs* RHE plotted as CV cycle numbers of PCN@N-graphene film (inset is the current density@−0.2 V *vs* RHE).

obtained in the high frequency zone and then used to correct the polarization curves. The charge transfer resistance (R_{ct}) is related to the electrocatalytic kinetics and its lower value corresponds to the faster reaction rate, which can be obtained from the semicircle in the low frequency zone. The R_{ct} value for PCN@N-graphene-750 is about 35.4 Ω cm^2, which is much lower than that of other materials with over one hundred Ω cm^2, suggesting the easiest electron transfer, and consequently, the most favorable HER kinetics at the PCN@N-graphene-750/electrolyte interface. The R_{ct} value of as-prepared films decreases after N-doping, indicating that the HER kinetics is improved significantly by N-doping.

HER Durability. Durability is another important criterion to evaluate the electrocatalyst performance; so the cycle performance was investigated using polarization curves (Figure 4e, without *iR* correction). Surprisingly, the HER activity of PCN@N-graphene film increases at first: the current density J at −0.6 V *vs* RHE ($j_{-0.6}$) increases from 45.9 mA cm^{-2} to 101.7 mA cm^{-2} and η_o changes from −0.034 V to −0.010 V *vs* RHE after 750 cycles. Then HER activity slightly decreases, and η_o does not change much but $j_{-0.6}$ decreases gradually to 97.4 mA cm^{-2} after 1000 cycles, to 88.3 mA cm^{-2} after 4000 cycles and to 87.8 mA cm^{-2} after 5000 cycles. Therefore, the PCN@N-graphene film still

maintains 86.3% of the highest $j_{-0.6}$ after 5000 cycles, displaying an excellent durability.[9,10,33,44] Moreover, η_{10} *vs* CV cycle numbers decreases greatly at the initial 750 cycles and increases slightly after 5000 cycles, achieving the lowest value at 750 cycles (0.08 V, Figure 4f). The $j_{-0.2}$ current density displays the opposite trend as compared to that of η_{10}, obtaining the highest value at 750 CV cycles (27.2 mA cm^{-2}, inset of Figure 4f). The variation of η_{10} and $j_{-0.2}$ is consistent with polarization curves, confirming the excellent durability of this heterostructured film. Significantly, the layer-by-layer and hierarchical porous microstructure can still be preserved after 5000 cycles (Figure S14). The superior durability of PCN@N-graphene film can be related to the flexibility and stiffness of the freeze-dried film, its special hierarchical porous structure and the strong coupling between PCN nanolayers and N-graphene sheets.

Effect of PCN Nanolayers Percentage on the HER Activity. Effect of the percentage of PCN nanolayers in the hybrid film on the HER activity has been studied (Figure S15, not *iR* corrected). First, the HER activity of the hybrid films increases with the content of PCN nanolayers increasing from zero to 5% and further to 9.1%, and then decreases with further increasing the content of PCN nanolayers to 25 and 50%. The hybrid film with 9.1% of PCN nanolayers (that is PCN@N-graphene wet film with η_o of −0.26 V and $j_{-0.6}$ of 20.6 mA cm^{-2}) exhibits the best HER activity. Therefore, the percentage of PCN nanolayers in the hybrid films is highly important for optimizing the HER activity, which is related to the amount of active sites, electron transfer resistance and interactions between PCN nanolayers and N-graphene sheets.

Relationship between the Composition, Microstructure of Catalysts and HER Performance. By integrating PCN nanolayers with graphene into a heterostructure, strong coupling between PCN nanolayers and graphene sheets is probably formed *via* oxygen groups and defective sites, which can compromise a part of electrostatic repulsive forces of graphene sheets. So there is a small reduction in interlayer distance and specific surface area of the hybrid film. It is well-known that maximizing the exposed catalytic active sites is a facile approach to optimize the catalytic activity. Bulk C_3N_4 exposes little active sites due to the small surface area and limited number of exposed edges. 2D C_3N_4 nanolayers can expose active sites at the edges, but the in-plane macropores in PCN nanolayers can expose much more active sites thus maximizing the exposed HER active sites in 2D PCN nanolayers. Thereby, in spite of the decreased surface area, the HER activities of the heterostructures studied (PCN@graphene and PCN@N-graphene films) are still better than those of pure graphene and N-graphene films because of the more exposed active sites.

In addition, hierarchical pores were generated intra and inter layer in the films due to the interlocking-tile cross-linking and the corrugated configuration of graphene sheets and PCN nanolayers.[46] The hierarchical porous structure enhances its high surface area and is also highly facile for the mass transport during HER processes. Especially, it can accommodate the volume change during gas evolution, thus preventing the degradation of microstructure and catalyst peeling, which guarantees a robust durability.

During N-doping process, graphene sheets and PCN nanolayers agglomerated due to the elevated temperature and high pressure, and the residual oxygen functional groups on graphene prepared by Hummers' method can be eliminated further. Consequently, the interlayer distance and specific surface area decreased, but the electron conductivity increased greatly. Moreover, introducing N into carbon structure results in asymmetry spin and charge density distribution, which are beneficial for the electrocatalytic process. Therefore, the HER activity of N-doped film (PCN@N-graphene and N-graphene films) is higher than that of non-N-doped film (PCN@graphene and graphene films).

There was a drastic enhancement of the HER activity for PCN@N-graphene film during CV cycles, in which j_0 increased from 0.37 at the beginning to 0.43 mA cm^{-2} after 750 CV cycles, η_{10} decreased from 0.17 to 0.08 V and the Tafel slope decreased from 88.6 mV dec^{-1} to 49.1 mV dec^{-1} These results suggest a change in the HER mechanism during the CV cycles, in which the RDS changed from Volmer step at the beginning to Heyrovsky step after 750 cycles. The wetting ability of the dried film (PCN@N-graphene film) was very poor due to the removal of oxygen groups upon drying, so at the beginning of the HER process the contact and electron transfer at the electrode/electrolyte interface were not good, making the primary discharge step very slow. After some CV cycles, the interactions between active species, the dried film and electrolyte were enhanced, so the contact and the electron transfer at the interface were improved significantly. Thereby, the discharge process became quick, and the RDS changed to the desorption process of hydrogen on the film (Heyrovsky step). With the highest j_0 and smallest Tafel slope, PCN@N-gaphene-750 exhibits the best HER performance among all the samples.

CONCLUSIONS

In summary, this work reports the first design and fabrication of 3D N-graphene-C_3N_4 hybrid film with the microstructure comparable to van der Waals heterostructures. The novel material studied exhibited an excellent catalytic activity, which makes it an ideal candidate for the next generation of HER catalysts. Further study revealed that the performance enhancement can be associated with excellent structural properties of electrocatalysts, *i.e.*, abundance of exposed

active sites, hierarchical porous structure, synergistic coupling between PCN nanolayers and graphene sheets, and nitrogen doping modification of graphene functionality. The resulting catalyst also showed an excellent durability during long-term cycling in acidic environment due to the effective accommodation of C_3N_4 between graphene sheets. Moreover, this material was prepared *via* a facile procedure using low-cost precursors, which can be easily extended to the preparation of other graphene-based 3D catalysts for a broad range of applications such as heterocatalysis, solar cells, fuel cells, *etc*.

EXPERIMENTAL SECTION

Materials Synthesis. PCN was prepared using packed silica spheres (~120 nm, see Supporting Information for preparation process) as hard templates. In a typical procedure, 1 g of packed SiO_2 spheres were put into 1 g of melted cyanamide, and the mixture was kept in a vacuum oven at 50 °C for 3 h. Then the mixture was subjected to annealing in N_2 at 550 °C with a ramp of 4 °C min^{-1} for 5.5 h in a tube furnace (Elite Thermal Systems, Ltd.). 0.1 g of the as-obtained product was etched using 2 mL of 5 M NaOH aqueous solution at room temperature overnight, washed with DI water three times and dried under ambient conditions. For the purpose of comparison, bulk g-C_3N_4 without macropores was also prepared by direct annealing cyanamide in N_2 at 550 °C with a ramp of 4 °C min^{-1} for 5.5 h.

To prepare 2D PCN nanolayers, 1 mg mL^{-1} of PCN aqueous suspension was subjected to bath-sonication (185W, Branson) for 4 h, followed by centrifugation at 1000 rpm for 60 min. The top 80% liquid was collected, which was the aqueous suspension of PCN nanolayers. C_3N_4 nanolayers without macropores were prepared similarly by sonicating 1 mg mL^{-1} of bulk g-C_3N_4 aqueous suspension for 4 h and centrifuging the as-resultant product at 1000 rpm for 60 min.

Furthermore, hybrid films were fabricated by a vacuum filtration method. Specifically, 0.91 mg of PCN nanolayer suspension (~0.43 mg mL^{-1}) and 9.09 mg of 0.5 mg mL^{-1} graphene oxide solution (see Supporting Information for preparation process) were mixed and diluted into 100 mL of 0.1 mg mL^{-1} PCN@GO suspension. After adding 350 μL of ammonia (25%), the mixture was bath-sonicated for 1 h to produce a homogeneously mixed suspension. After further addition of 40 μL of hydrazine, the PCN@GO suspension was reduced to PCN@graphene suspension at 95 °C for 6 h by ammonia and hydrazine. Then it was vacuum-filtrated using a mixed cellulose esters membrane filter (47 mm in diameter, 0.22 mm pore size, Whatman) to form a hybrid film, which was peeled off from the filter membrane and freeze-dried into PCN@graphene film. Pure graphene film was prepared similarly; sonicating 100 mL of 0.1 mg mL^{-1} GO solution for 1 h, reducing it using 350 μL of ammonia and 40 μL of hydrazine at 95 °C for 6 h, then filtrating the reduced solution and freeze-drying the peeled film.

Lastly, PCN@N-graphene film was synthesized by solvothermal treating of PCN@graphene film in a stainless steel autoclave with 10 mL of ammonia at 150 °C for 5 h, and then freeze-dried. For the purpose of comparison, N-graphene film was also prepared through the same solvothermal process at 150 °C for 5 h in 10 mL of ammonia (25%) using pure graphene film.

Electrochemical Testing. Electrochemical measurements were performed in a three-electrode glass cell on a 760 workstation (Pine Research Instruments, US) using Ag/AgCl/KCl as the reference electrode, graphite rod as the counter electrode and hybrid films as working electrodes. All measurements were carried out in N_2-saturated 0.5 M H_2SO_4 to eliminate dissolved oxygen. All potentials were referenced to a RHE by adding a value of (0.205 + 0.059 × pH) V.

Characterization. Morphology of as-obtained samples was observed using TEM (Tecnai G2 Spirit) and SEM (QUANTA 450). EDS spectra were measured on the QUANTA 450 SEM. Atomic force microscopy (AFM) analysis was conducted on a NT-MDT Ntegra Solaris machine. XRD patterns were recorded on a Philips 1130 X-ray diffractometer (40 kV, 25 mA, Cu Kα radiation, λ = 1.5418 Å). Raman spectra were recorded on an iHR550 Raman microscope (HORIBA scientific) with 532 nm solid laser as an excitation source. FTIR spectroscopy was recorded on a Nicolet 6700 spectrometer. UV−vis absorption spectra were obtained using a SHIMADZU UV-2600 spectrophotometer. TGA (Setaram) was operated from 20 to 800 °C with a ramp of 10 °C·min^{-1} under N_2/O_2 flow. XPS spectra were recorded on an Axis Ultra (Kratos Analytical, UK) with an Al Ka source (1486.6 eV). Nitrogen adsorption−desorption isotherms were measured at −196 °C on a TriStar II 3020 Micrometrics apparatus. Adsorption of MB from ethanol solution was also used to measure the surface area (see Supporting Information).

Conflict of Interest: The authors declare no competing financial interest.

Acknowledgment. This work was financially supported by the Australian Research Council (ARC) through the Discovery Project program (DP 130104459, DP 140104062).

Supporting Information Available: Experimental sections include the preparation of graphene oxide and silica template; electrochemical testing method and details of the specific surface area measurements; characterization of the morphology, structure, and composition of as-prepared materials and commercial Pt/CF; electrochemical cell and HER performance testing of as-prepared materials. This material is available free of charge *via* the Internet at http://pubs.acs.org.

REFERENCES AND NOTES

1. Turner, J. A. Sustainable Hydrogen Production. *Science* **2004**, *305*, 972–974.
2. Thomas, J. G. N. Kinetics of Electrolytic Hydrogen Evolution and the Adsorption of Hydrogen by Metals. *Trans. Faraday Soc.* **1960**, 1603–1611.
3. Leonard, K. C.; Bard, A. J. Pattern Recognition Correlating Materials Properties of the Elements to Their Kinetics for the Hydrogen Evolution Reaction. *J. Am. Chem. Soc.* **2013**, *135*, 15885–15889.
4. Trasatti, S. Work Function, Electronegativity, and Electrochemical Behaviour of Metals III. Electrolytic Hydrogen Evolution in Acid Solutions. *J. Electroanal. Chem.* **1972**, *39*, 163–184.
5. Wang, Z. L.; Yan, J. M.; Ping, Y.; Wang, H. L.; Zheng, W. T.; Jiang, Q. An Efficient CoAuPd/C Catalyst for Hydrogen Generation from Formic Acid at Room Temperature. *Angew. Chem., Int. Ed.* **2013**, *52*, 4406–4409.
6. Navarro-Flores, E.; Chong, Z.; Omanovic, S. Characterization of Ni, NiMo, NiW and NiFe Electroactive Coatings as Electrocatalysts for Hydrogen Evolution in an Acidic Medium. *J. Mol. Catal. A: Chem.* **2005**, *226*, 179–197.
7. Furuya, N.; Motoo, S. The Electrochemical Behavior of Ad-Atoms and Their Effect on Hydrogen Evolution Part III. Platinum Ad-Atoms on Gold, and Gold Ad-Atoms on Platinum. *J. Electroanal. Chem.* **1978**, *88*, 151–160.
8. Laursen, A. B.; Varela, A. S.; Dionigi, F.; Fanchiu, H.; Miller, C.; Trinhammer, O. L.; Rossmeisl, J.; Dahl, S. Electrochemical Hydrogen Evolution: Sabatier's Principle and the Volcano Plot. *J. Chem. Educ.* **2012**, *89*, 1595–1599.
9. Zhuo, J.; Wang, T.; Zhang, G.; Liu, L.; Gan, L.; Li, M. Salts of $C_{60}(OH)_8$ Electrodeposited onto a Glassy Carbon Electrode: Surprising Catalytic Performance in the Hydrogen Evolution Reaction. *Angew. Chem., Int. Ed.* **2013**, *52*, 10867–10870.

10. Xu, Y. F.; Gao, M. R.; Zheng, Y. R.; Jiang, J.; Yu, S. H. Nickel/Nickel(II) Oxide Nanoparticles Anchored onto Cobalt(IV) Diselenide Nanobelts for the Electrochemical Production of Hydrogen. *Angew. Chem., Int. Ed.* **2013**, *52*, 8546–8550.
11. Voiry, D.; Yamaguchi, H.; Li, J. W.; Silva, R.; Alves, D. C. B.; Fujita, T.; Chen, M. W.; Asefa, T.; Shenoy, V. B.; Eda, G.; *et al.* Enhanced Catalytic Activity in Strained Chemically Exfoliated WS_2 Nanosheets for Hydrogen Evolution. *Nat. Mater.* **2013**, *12*, 850–855.
12. Sathe, B. R.; Zou, X.; Asefa, T. Metal-Free B-Doped Graphene with Efficient Electrocatalytic Activity for Hydrogen Evolution Reaction. *Catal. Sci. Technol.* **2014**, *4*, 2023–2030.
13. Wang, H.; Lu, Z.; Kong, D.; Sun, J.; Hymel, T. M.; Cui, Y. Electrochemical Tuning of MoS_2 Nanoparticles on Three-Dimensional Substrate for Efficient Hydrogen Evolution. *ACS Nano* **2014**, *8*, 4940–4947.
14. Das, R. K.; Wang, Y.; Vasilyeva, S. V.; Donoghue, E.; Pucher, I.; Kamenov, G.; Cheng, H. P.; Rinzler, A. G. Extraordinary Hydrogen Evolution and Oxidation Reaction Activity from Carbon Nanotubes and Graphitic Carbons. *ACS Nano* **2014**, *8*, 8447–8456.
15. Geim, A. K.; Grigorieva, I. V. Van Der Waals Heterostructures. *Nature* **2013**, *499*, 419–425.
16. Zheng, Y.; Jiao, Y.; Zhu, Y.; Li, L. H.; Han, Y.; Chen, Y.; Du, A.; Jaroniec, M.; Qiao, S. Z. Hydrogen Evolution by a Metal-Free Electrocatalyst. *Nat. Commun.* **2014**, *5*, 3783.
17. Hinnemann, B.; Moses, P. G.; Bonde, J.; Jørgensen, K. P.; Nielsen, J. H.; Horch, S.; Chorkendorff, I.; Nørskov, J. K. Biomimetic Hydrogen Evolution MoS_2 Nanoparticles as Catalyst for Hydrogen Evolution. *J. Am. Chem. Soc.* **2005**, *127*, 5308–5305.
18. Ivanovskaya, A.; Singh, N.; Liu, R. F.; Kreutzer, H.; Baltrusaitis, J.; Nguyen, T. V.; Metiu, H.; McFarland, E. Transition Metal Sulfide Hydrogen Evolution Catalysts for Hydrobromic Acid Electrolysis. *Langmuir* **2013**, *29*, 480–492.
19. Yang, X.; Cheng, C.; Wang, Y.; Qiu, L.; Li, D. Liquid-Mediated Dense Integration of Graphene Materials for Compact Capacitive Energy Storage. *Science* **2013**, *341*, 534–537.
20. Ji, H.; Zhang, L.; Pettes, M. T.; Li, H.; Chen, S.; Shi, L.; Piner, R.; Ruoff, R. S. Ultrathin Graphite Foam: A Three-Dimensional Conductive Network for Battery Electrodes. *Nano Lett.* **2012**, *12*, 2446–2451.
21. El-Kady, M. F.; Strong, V.; Dubin, S.; Kaner, R. B. Laser Scribing of High-Performance and Flexible Graphene-Based Electrochemical Capacitors. *Science* **2012**, *335*, 1326–1330.
22. Dikin, D. A.; Stankovich, S.; Zimney, E. J.; Piner, R. D.; Dommett, G. H.; Evmenenko, G.; Nguyen, S. T.; Ruoff, R. S. Preparation and Characterization of Graphene Oxide Paper. *Nature* **2007**, *448*, 457–460.
23. Chen, H.; Müller, M. B.; Gilmore, K. J.; Wallace, G. G.; Li, D. Mechanically Strong, Electrically Conductive, and Biocompatible Graphene Paper. *Adv. Mater.* **2008**, *20*, 3557–3561.
24. Yang, X.; Zhu, J.; Qiu, L.; Li, D. Bioinspired Effective Prevention of Restacking in Multilayered Graphene Films: Towards the Next Generation of High-Performance Supercapacitors. *Adv. Mater.* **2011**, *23*, 2833–2838.
25. Chen, S.; Qiao, S. Z. Hierarchically Porous Nitrogen-Doped Graphene-$NiCo_2O_4$ Hybrid Paper as an Advanced Electrocatalytic Water-Splitting Material. *ACS Nano* **2013**, *7*, 10190–10196.
26. Chen, S.; Duan, J. J.; Ran, J. R.; Jaroniec, M.; Qiao, S. Z. N-Doped Graphene Film-Confined Nickel Nanoparticles as a Highly Efficient Three-Dimensional Oxygen Evolution Electrocatalyst. *Energy Environ. Sci.* **2013**, *6*, 3693–3699.
27. Schwinghammer, K.; Mesch, M. B.; Duppel, V.; Ziegler, C.; Senker, J.; Lotsch, B. V. Crystalline Carbon Nitride Nanosheets for Improved Visible-Light Hydrogen Evolution. *J. Am. Chem. Soc.* **2014**, *136*, 1730–1733.
28. Duan, J.; Zheng, Y.; Chen, S.; Tang, Y.; Jaroniec, M.; Qiao, S. Mesoporous Hybrid Material Composed of Mn_3O_4 Nanoparticles on Nitrogen-Doped Graphene for Highly Efficient Oxygen Reduction Reaction. *Chem. Commun.* **2013**, *49*, 7705–7707.
29. Chai, B.; Liao, X.; Song, F.; Zhou, H. Fullerene Modified C_3N_4 Composites with Enhanced Photocatalytic Activity under Visible Light Irradiation. *Dalton Trans.* **2014**, *43*, 982–989.
30. Kim, M.; Hwang, S.; Yu, J.-S. Novel Ordered Nanoporous Graphitic C_3N_4 as a Support for Pt-Ru Anode Catalyst in Direct Methanol Fuel Cell. *J. Mater. Chem.* **2007**, *17*, 1656.
31. Yan, S. C.; Li, Z. S.; Zou, Z. G. Photodegradation Performance of G- C_3N_4 Fabricated by Directly Heating Melamine. *Langmuir* **2009**, *25*, 10397–10401.
32. Zhang, J.; Zhu, Z.; Tang, Y.; Mullen, K.; Feng, X. Titania Nanosheet-Mediated Construction of a Two-Dimensional Titania/Cadmium Sulfide Heterostructure for High Hydrogen Evolution Activity. *Adv. Mater.* **2014**, *26*, 734–738.
33. Xie, J.; Zhang, H.; Li, S.; Wang, R.; Sun, X.; Zhou, M.; Zhou, J.; Lou, X. W.; Xie, Y. Defect-Rich MoS_2 Ultrathin Nanosheets with Additional Active Edge Sites for Enhanced Electrocatalytic Hydrogen Evolution. *Adv. Mater.* **2013**, *25*, 5807–5813.
34. Laursen, A. B.; Vesborg, P. C.; Chorkendorff, I. A High-Porosity Carbon Molybdenum Sulphide Composite with Enhanced Electrochemical Hydrogen Evolution and Stability. *Chem. Commun.* **2013**, *49*, 4965–4967.
35. Chang, Y. H.; Lin, C. T.; Chen, T. Y.; Hsu, C. L.; Lee, Y. H.; Zhang, W.; Wei, K. H.; Li, L. J. Highly Efficient Electrocatalytic Hydrogen Production by MoS_x Grown on Graphene-Protected 3D Ni Foams. *Adv. Mater.* **2013**, *25*, 756–760.
36. McAllister, M. J.; Li, J. L.; Adamson, D. H.; Schniepp, H. C.; Abdala, A. A.; Liu, J.; Herrera-Alonso, M.; Milius, D. L.; Car, R.; Prud'homme, R. K.; *et al.* Single Sheet Functionalized Graphene by Oxidation and Thermal Expansion of Graphite. *Chem. Mater.* **2007**, *19*, 4396–4404.
37. Choucair, M.; Thordarson, P.; Stride, J. A. Gram-Scale Production of Graphene Based on Solvothermal Synthesis and Sonication. *Nat. Nanotechnol.* **2009**, *4*, 30–33.
38. Li, Y.; Wang, H.; Xie, L.; Liang, Y.; Hong, G.; Dai, H. MoS_2 Nanoparticles Grown on Graphene: An Advanced Catalyst for the Hydrogen Evolution Reaction. *J. Am. Chem. Soc.* **2011**, *133*, 7296–7299.
39. Chen, Z.; Cummins, D.; Reinecke, B. N.; Clark, E.; Sunkara, M. K.; Jaramillo, T. F. Core-Shell MoO_3-MoS_2 Nanowires for Hydrogen Evolution: A Functional Design for Electrocatalytic Materials. *Nano Lett.* **2011**, *11*, 4168–4175.
40. Xie, J.; Zhang, J.; Li, S.; Grote, F.; Zhang, X.; Zhang, H.; Wang, R.; Lei, Y.; Pan, B.; Xie, Y. Controllable Disorder Engineering in Oxygen-Incorporated MoS_2 Ultrathin Nanosheets for Efficient Hydrogen Evolution. *J. Am. Chem. Soc.* **2013**, *135*, 17881–17888.
41. Merki, D.; Hu, X. Recent Developments of Molybdenum and Tungsten Sulfides as Hydrogen Evolution Catalysts. *Energy Environ. Sci.* **2011**, *4*, 3878.
42. Lukowski, M. A.; Daniel, A. S.; Meng, F.; Forticaux, A.; Li, L.; Jin, S. Enhanced Hydrogen Evolution Catalysis from Chemically Exfoliated Metallic MoS_2 Nanosheets. *J. Am. Chem. Soc.* **2013**, *135*, 10274–10277.
43. Zheng, Z.; Li, N.; Wang, C.-Q.; Li, D.-Y.; Meng, F.-Y.; Zhu, Y.-M.; Li, Q.; Wu, G. Electrochemical Synthesis of Ni-S/CeO_2 Composite Electrodes for Hydrogen Evolution Reaction. *J. Power Sources* **2013**, *230*, 10–14.
44. Cao, B.; Veith, G. M.; Neuefeind, J. C.; Adzic, R. R.; Khalifah, P. G. Mixed Close-Packed Cobalt Molybdenum Nitrides as Non-Noble Metal Electrocatalysts for the Hydrogen Evolution Reaction. *J. Am. Chem. Soc.* **2013**, *135*, 19186–19192.
45. Liao, L.; Zhu, J.; Bian, X.; Zhu, L.; Scanlon, M. D.; Girault, H. H.; Liu, B. MoS_2 formed on Mesoporous Graphene as a Highly Active Catalyst for Hydrogen Evolution. *Adv. Funct. Mater.* **2013**, *23*, 5326–5333.
46. Qiu, L.; Zhang, X.; Yang, W.; Wang, Y.; Simon, G. P.; Li, D. Controllable Corrugation of Chemically Converted Graphene Sheets in Water and Potential Application for Nanofiltration. *Chem. Commun.* **2011**, *47*, 5810–5812.